Fano Resonance Engineering in Mirror-Symmetry-Broken THz Metamaterials

Xuefeng Li,[1] Xinya Bian,[1] William I. Milne,[1] and Daping Chu,[1,*]

[1]*Electrical Engineering Division, Department of Engineering, University of Cambridge, 9 JJ Thomson Avenue, Cambridge CB3 0FA, UK*

**Corresponding author: dpc31@cam.ac.uk*

We introduce a comprehensive approach to the design of mirror-symmetry broken terahertz (THz) metamaterials and present both the simulation and experimental results which show the desired asymmetric Fano resonances and electromagnetic induced transparency (EIT)-like windows. With a full wave simulation, we find these asymmetry-induced resonance modes possess extremely high quality factors and they broaden with increase of the structure asymmetry. This phenomenon arises from the destructive interference of a super-radiative bright mode and a sub-radiative dark mode which can't be excited directly. Surface current and electric field distributions are analyzed to explain the emergence of these Fano resonances. An intuitive mechanical coupled oscillator model is derived to explain the unique line-shape of such Fano resonances. Moreover, large resonant frequency tuning (50 GHz) of Fano resonance has been demonstrated by temperature induced phase change in liquid crystals. We believe that the Fano resonance in THz metamaterials may serve as a strong building block for passive or active THz elements with potential applications for future detection and sensing systems and devices.

OCIS codes: 300.6495, 160.3710, 160.3918, 260.5740.

1. INTRODUCTION

The terahertz (THz) spectrum, which spans the gap between microwave and infrared frequencies, has drawn increasing attention over the past two decades [1–4]. Due to the unique interaction between THz radiation and materials, innumerable material characteristic responses are being exploited, including lattice vibration [5], rotation transition of molecules [6] and intra-band absorption in semiconductors [7]. This research work can enable THz technology to find its use in an increasingly wide range of applications such as sensing and communications [8,9]. However, efficient and reliable THz applications require not only high performance sources such as Quantum Cascade Lasers [10] and detectors or characterization method such as THz Time-Domain Spectroscopy (THz-TDS) [11], but also passive or active components which are essential for THz wave modulation.

In recent years, metamaterials [12–14] and meta-surfaces [15,16] have greatly expanded our knowledge by realizing intriguing physical phenomena. A variety of novel properties such as negative refraction [12] and cloaking [17] have been exploited extensively and demonstrated their potential in various applications. In electromagnetics, these characteristics can be attributed to a strong light-structure interaction and effective abnormal material parameters could be achieved with or without resonances [18]. Metamaterials are normally composed of designed units at sub-wavelength scale (~λ/10) and the incident radiation is coupled into the structure through resonance with high efficiency. In order to concentrate light in a sub-wavelength structure, sharp resonances or modes should be excited which support high quality factor (Q-factor) [19]. Confinement of light can be engineered with the reduction of radiation loss (coupling to free space). However, resonances in standard symmetric metamaterials such as split-ring resonators are usually coupled to the far field, which leads to high radiation loss and low Q-factor [20]. Several mechanisms have been proposed and demonstrated to achieve sharp Fano responses by breaking the structure symmetry [21–23]. Nevertheless, previous studies are mainly focused on simple structures [24–27] and a systematic engineering of Fano resonances are needed to improve the performance and to add more flexibility. Fano resonances were originally found in quantum physics and have an asymmetric line-shape instead of a symmetric Lorentzian one. In metamaterials, Fano resonances are attributed to the constructive or destructive interference of a low Q-factor bright mode with a narrow distinctive dark mode [23,28]. Due to the sharp response nature of Fano resonances, a small perturbation in material or environment can lead to huge shifts. This property can be exploited in a range of applications, such as label-free detection and sensing [29].

In this paper, we demonstrate Fano resonances and EIT-like phenomenon arising from structural asymmetry in THz metamaterials. A number of resonant structures with different configurations are simulated and analysed. Six basic structures are chosen to include most of the planar metamaterials reported and asymmetry is introduced in both in-plane directions. Fano resonances can be observed even when the slightest degree of asymmetry is introduced in these structures. Compared with normal symmetric metamaterials, we focus on new transmission peaks and dips which are attributed to the coupling of a bright radiation mode and dark mode. Furthermore, a theoretical coupled-oscillator model is used to explain the asymmetric transmission line-shape induced by bright/dark mode coupling. Lastly, we study the thermal tunability of a liquid crystal infiltrated symmetry-breaking THz metamaterials and demonstrate large Fano resonant frequency shift (50 GHz) controlled by temperature.

2. SAMPLE DESIGN

The metamaterial structures employed in this work are based upon a recently presented electric analogue to the split-ring resonators (eSRRs) [30,31]. The 3D schematic illustration of

different configurations is shown in Fig. 1*(a-f)* and these six geometries are denoted as Structures *(a)* to *(f)* correspondingly in this paper. All of the structures are composed of sub-wavelength unit cells, which have the same in-plane period of 50 μm, outer dimension of 36 μm, line width of 4 μm and gap width of 2 μm. These metamaterials are composed of gold and sit on highly transparent substrates in the THz region. The thickness of the designed metamaterials is set to be 2 μm, which is much larger than the skin depth of gold in THz spectrum. Unlike in the optical region, these designed structure can easily be fabricated with standard micro-fabrication techniques, such as photolithography and e-beam lithography.

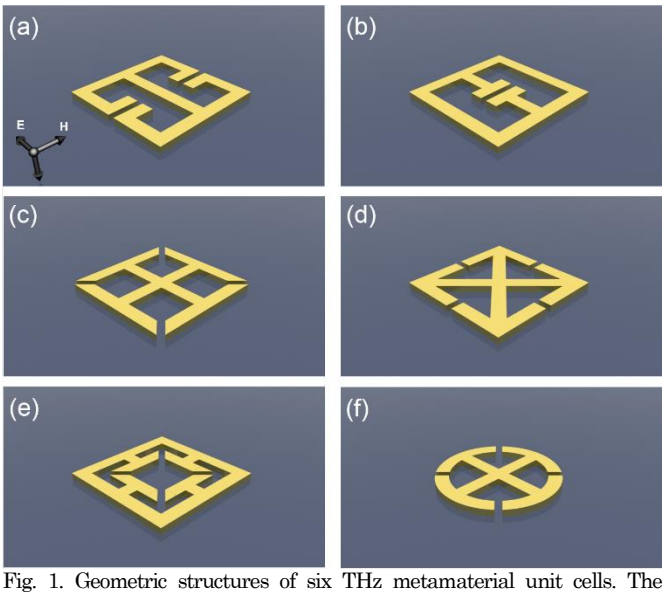

Fig. 1. Geometric structures of six THz metamaterial unit cells. The polarization state for all incident THz waves is shown in (a).

Structure *(a-f)* share similar topological geometries except the detailed format of air gap and metal bars, which are effective capacitors and inductors in an equivalent electric circuit model. The Ohmic losses of gold is neglected in THz region compared to optical region and the metal behaves like a perfect conductor. All six geometries are analyzed using commercially available full-wave electromagnetic simulation software (Lumerical FDTD Solutions v8.6). The mesh size in the x-y plane is set to be two orders less than the unit cell size and periodic boundary conditions are introduced to mimic the translational symmetry. Asymmetries in the x or y axis are inserted into these metamaterials by moving part of the unit cell in one direction or another (Fig. 2 right column). It should be mentioned that only one polarization state and normal incidence is considered in this work for simplicity. Simulated transmission spectra for corresponding symmetric and asymmetric structures are shown in the left column of Fig. 2.

In symmetric THz eSRRs, inductive capacitive (LC) resonance, dipole and higher order resonances can be observed as transmission dips (Fig. 2 (a-f) black lines). The LC resonance is due to inductive currents circulating around the ring perimeter combined with capacitive charge accumulation at the ring gaps. In contrast, the dipole and higher order resonances are due to antenna-like couplings between the eSRR metal parallel to the E-field. The dipole mode, as a fundamental mechanism to realize resonance peak in plasmonics, could easily couple to the far-field. Thus the FWHM of the dipole resonance is rather broadband compared to the LC or higher order resonances. When mirror symmetry is broken in either the *x* or *y* direction, all these structures exhibit new resonance peaks and dips in different frequencies or approximate positions near the original symmetric ones. For example, when the central metal bar of Structure *(a)* is moved 4 μm in the positive *x* direction (red line in Fig. 2(a)), the resonance dips still exist at the same positions as the original LC and dipole modes. The LC resonance at 0.53 THz is slightly red-shifted due to the coupling between the central bar and the side conductors. More importantly, a new sharp asymmetric resonance can be observed at 0.80 THz. Also moving the side gaps by 4 μm in positive y direction while keeping the mirror symmetry in the *x* direction (blue line in Fig. 2(a)) also generates new resonances at 1.48 THz (dip) and 1.53 THz (peak). These new features share a similar asymmetric line-shape as the Fano resonances, which is mostly caused by the interference between a directly excited bright mode and an indirectly excited dark mode. In Structure *(b)*, asymmetry in both x and y axis introduce similar Fano resonance line-shape at frequencies near the original dipole mode at 1.81 THz. The bandwidth of the Fano resonance generated by asymmetry in x direction is much narrower than the on caused by asymmetry in y direction. Symmetric structures of *(c-f)* are polarization insensitive due to their fourfold rotational symmetry C4. Therefore, analysis of the asymmetries introduced in these configurations are equivalent between transverse electric (TE) and transverse magnetic (TM) polarizations, which are orthogonal to each other. Structure (*c*) with broken symmetry in *x* direction exhibits similar sharp resonances at 1.55 THz. Interestingly, breaking mirror symmetry in the *y* axis causes the splitting of the LC mode and a highly-transparent window is opened between these resonant dips. This phenomenon resembles an electromagnetic induced transparency (EIT), in which the strong dispersion could lead to slow light or stopped light effect. In contrast to the structure *(c)*, the structure *(d)* shows a narrower EIT-like window for the LC mode with x-axis asymmetry and another sharp Fano resonance near the original transmission maximum at 1.34 THz. The Structures *(e)* and *(f)* display comparable Fano resonances all across the THz spectrum. Based on the line-shape and location of these new appearing resonances, we are able to classify them into three categories: single dip developed near the original transparent region (e.g. red line Fig. 2(a)), asymmetric line-shape far from any original resonances (e.g. blue line Fig. 2(a)), and EIT transparency window on or close to resonances dips in symmetric structures (e.g. blue line Fig. 2(c)). In order to gain deeper insight into the resonance mechanisms caused by breaking of the structural mirror symmetry, we analyze the electric field and surface current distribution for these typical resonances.

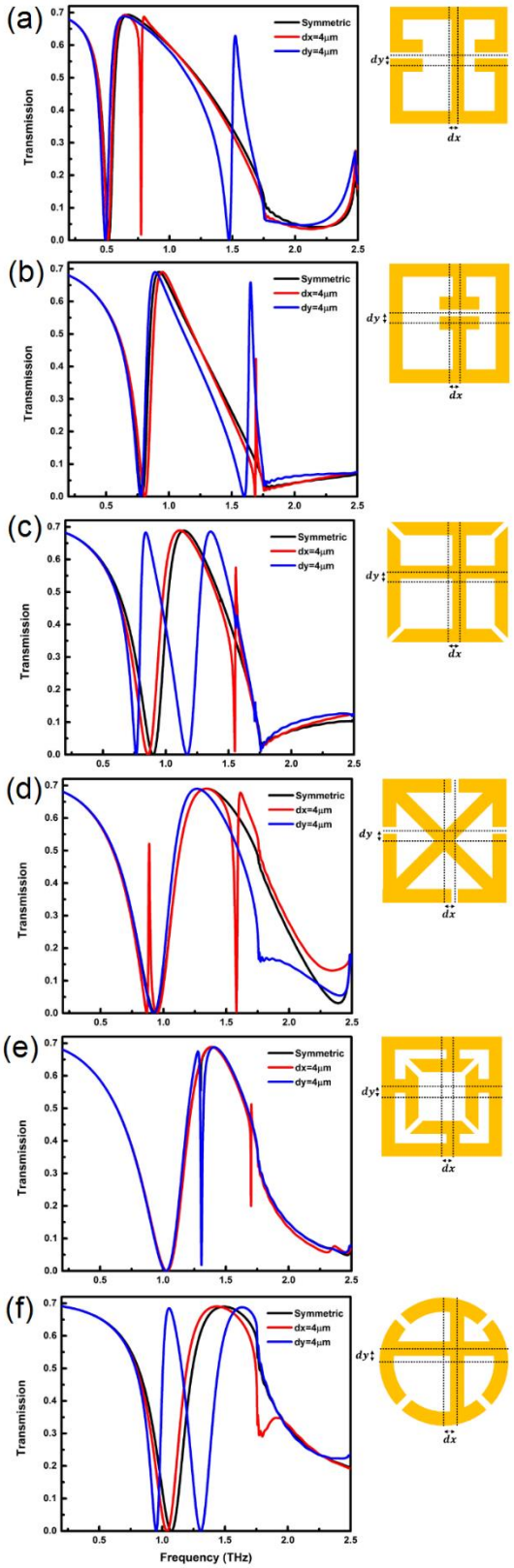

Fig. 2. Illustration of mirror symmetry broken (gold patterns) in x and y direction and corresponding transmission spectrums for both symmetric and asymmetric of structures *(a-f)*. The black, red and blue lines in the transmission spectrum stand for the symmetric, x-axis asymmetric and y-axis asymmetric circumstances, respectively.

3. DISCUSSION

Here without loss of generality and for the sake of simplicity in the proof of concept, we study the field distribution at typical resonances of structure *(a)* and *(c)*, which includes all three representative Fano resonances discussed above. As shown in Fig. 3, simulated electric field and surface current distributions of several typical resonances in asymmetric THz metamaterials *(a)* have been plotted. When symmetry in the x direction of structure *(a)* is broken, the intensity and position of the LC resonance at 0.52 THz remains the same as the symmetric case. The electric field and surface current at this resonance frequency are displayed in Fig. 3 (a) and (d), respectively. Similar to the symmetric situation, the electric field is confined in the two gaps and the surface current is composed of two enclosed loops with opposite rotating directions which possess zero net magnetic field. The ultra-sharp Fano resonance dip in the vicinity of the LC mode (0.80 THz), however, shows two closed loops of clockwise surface current (Fig. 3(e)), giving rise to non-zero net magnetic dipole moment oscillating perpendicular to the plane of the metamaterial. This specific resonance is related to a sub-radiant mode which couldn't be excited using symmetric unit cells. Due to the weak coupling to the continuum far-field radiation for the dark mode, a considerably larger current could be observed compared to that found in a normal super-radiant mode, which can easily couple to free space propagation wave. Also, the electric field (Fig. 3(b)) is confined in both gaps with much stronger intensity than for normal LC or dipole resonances in symmetric structures. This high-Q transmission dip can be attributed to the interference coupling between a broad super-radiant bright mode and a narrow sub-radiant dark mode. In this case, the bright mode is the transmission maximum and the dark mode is LC, as shown in Fig. 3(e). The coupling coefficient of these two distinct modes becomes non-zero when the structural symmetry is broken or when the propagation direction of the THz beam is not perpendicular to the metamaterial plane. Equivalently, introduction of unit symmetry breaking in the y direction will also produce the Fano resonance near 1.5 THz. Fig. 3(f) presents the surface current distributions for this asymmetric resonance dip at 1.48 THz. The location of this new resonance is on the slope of a highly radiating broad dipole mode (bright mode). However, instead of showing a parallel current for typical dipole resonances, the weak surface current clearly reveals a brand new mode. At the resonance dip, the currents oscillate coherently in each of the four sub-loops and the directions of these loop currents are clockwise in the upper-left and bottom-right sub-area, and anti-clockwise in the other two. (dark mode)

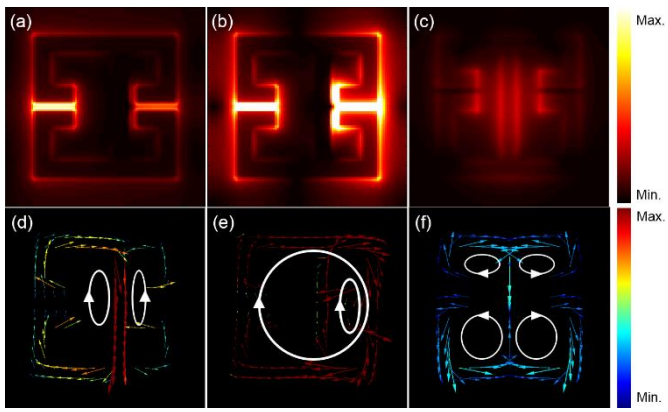

Fig. 3. Electric field (a-c) and surface current (d-f) distribution for typical symmetric Lorentzian and asymmetric Fano resonances for asymmetric Structure *(a)*.

The above Fano resonances have been developed either at transmission maximum or frequencies away from the symmetric Lorentzian resonances which correspond to typical LC, dipole or higher order modes. Interestingly, when the sub-radiant eigenmode is excited close to the super-radiant mode, an induced transparent window would open which is the classical analogue of EIT. As mentioned above, near fully transparency can be achieved in the middle of a LC resonance dip when mirror symmetry in y-direction is broken for the Structure *(c)*. This phenomenon can also be illustrated with regards to the electric field and surface current. Fig. 4(a) displays the electric field on the dipole resonance f=0.90 THz and the corresponding surface current is shown in Fig. 4(d) for the symmetric Structure *(c)*. Clearly, we can observe two currents loops with opposite direction for left and right parts, and the electric field is lightly confined in the four gaps in the corners (bright mode). The geometrical symmetry for the left and right contributes constructively to the LC mode at 0.90 THz. However, asymmetry in the y-direction breaks the mirror symmetry in this region and the previous degenerate resonance is split into two distinctive modes, as shown in Fig. 4(e) and (f). The splitting represents the LC resonances in each of the lower and upper parts (dark mode), respectively. Due to the geometrical difference, the resonant frequencies for the split dips are significantly separated from each other (0.76 THz and 1.17 THz). More importantly, a singular window is open with high THz transmission in the middle of these two resonance dips. This asymmetry generated EIT-like feature can also be associated with the destructive interference of a broad bright mode with a sharp dark mode.

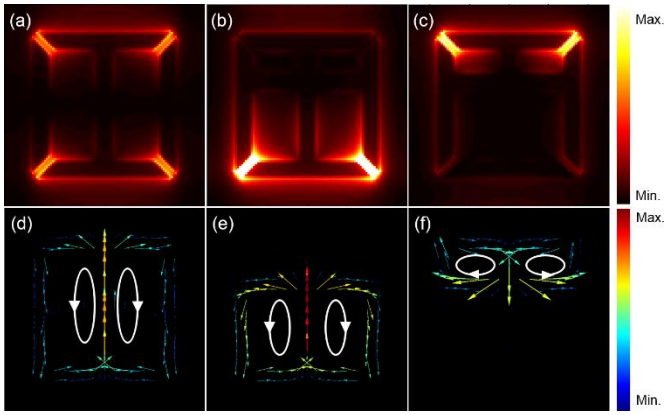

Fig. 4. Electric field (a-c) and surface current (d-f) distribution at EIT-like resonances when mirror-symmetry in y-direction is introduced for Structure *(c)*.

In order to investigate the active control of Fano resonances based on the degree of asymmetry, we discuss the evolution of the transmission spectrum and Q-factor in the Structure (a) with y-axis asymmetry. A parameter sweeping simulation for various asymmetry parameter is carried out, as shown in Fig. 5. As can be seen from Fig. 5(a) that Fano-like line-shape becomes predominant even when the slightest perturbation is introduced and the strength of the Fano resonance increases with the degree of asymmetry. With the increase in the geometrical asymmetric value, the width of the resonance broadens and a lower transmission dip is achieved. In order to study the broadening effect of the resonance, we define the normalized spectral width for Fano resonance as $NSW = \frac{f_{\max} + f_{\min}}{f_{\max} - f_{\min}} / 2$, where $f_{\max}$ and $f_{\min}$ are the frequency values on the resonance peak and dip, respectively. This value is equivalent to the Q-factor in Lorentizian resonances. Fig. 5(b) shows that the quality factor decreases with the degree of asymmetry in an exponential manner. When the gaps in Structure (a) are moved 1μm in y direction, a NSW factor as high as 152 can be achieved, which is more than an order of magnitude higher than normal symmetric resonances. However, Fano resonances in our metamaterial structures are very sensitive to both the fabrication procedures and the surrounding environment. As degree of asymmetry increases, the coupling between the metamaterial eigen-mode and free-space radiation mode becomes more predominant. This is the main reason for the expansion of max/min transmission difference and the line-shape [32]. This feature is not limited to asymmetric THz metamaterials, but is a common characteristic of Fano resonances. In addition, we also observe the central frequency shift of this newly emerged resonance. As the blue line shows in Fig.5 (b), the central frequency, which is defined as $f_{Fano=} \frac{f_{\max} + f_{\min}}{2}$, blue shifts with increase of structural asymmetry. However, this shift effect (either red or blue) is normally attributed to the specific structure of the unit cell and large asymmetry could lead to the frequency shift in either bright or dark modes.

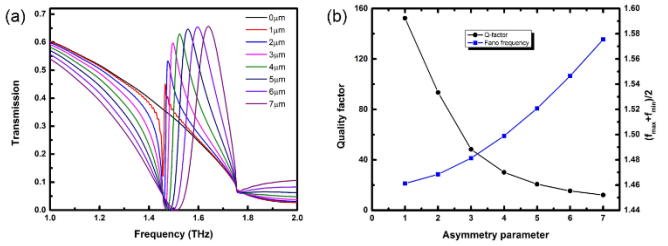

Fig. 5. (a) Transmission spectrum and (b) corresponding Q-factor of Fano resonance for different degree of *y*-axis asymmetry.

In addition, Fano resonances can also be tailored by changing other parameters while fixing the asymmetry factor in the metamaterial structure. For example, we fix the asymmetric parameter for Structure *(b)* and tune the length of the central bar *gx*, as shown in Fig. 6(a). This single parameter is able to red-shift the Fano resonances when the value of the central bar sweeps from 6 μm to 24 μm. The extra degree of freedom and flexibility provides another convenient way for THz modulation by using Fano resonances.

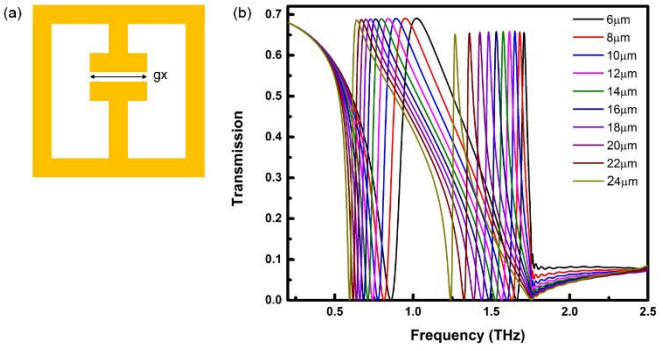

Fig. 6 (a) Structure *(b)* with asymmetry in y axis ($\Delta y = 4\mu m$) and tunable parameter gx. (b) Fano resonances arising from structure asymmetry can be controlled by sweeping the value of gx.

4. GENERAL DESCRIPTION

To better explain the Fano resonance and EIT phenomenon arising in asymmetric THz metamaterials, we develop a simple coupled oscillator model [33] to describe the physical mechanism. By introducing a general description of an inner-coupled metamaterial structure, we consider a hybrid system which is composed of two artificial harmonic oscillators, as shown in Fig. 7(a). The oscillation frequencies for these two unit elements are ω_1 and ω_2, and the damping rate γ_1 and γ_2 which represent the radiation losses, respectively. The coupling coefficient between these two oscillators is κ. In this case, we specifically assign the first element to be a super-radiative molecule which can be efficiently coupled with the incident field $E_0 e^{i\omega t}$ with high damping rate γ_1. While the other element is a sub-radiative molecule which weakly couples to the incident field and has a low damping rate γ_2. The complex amplitude of both molecules x_1 and x_2 can be described with following equations of motion:

$$\ddot{x}_1 + \gamma_1 \dot{x}_1 + \omega_1^2 x_1 + \kappa x_2 = E_0 e^{i\omega t} \quad (1)$$

$$\ddot{x}_2 + \gamma_2 \dot{x}_2 + \omega_2^2 x_2 + \kappa x_1 = 0 \quad (2)$$

Due to the harmonic nature of these two elements, the complex amplitude can be written as $x_1 = ae^{i\omega t}$ and $x_2 = be^{i\omega t}$. Because we can't evaluate the dark mode directly and the transmission spectrum is only valid in the far field case, the bright mode is analysed. After some simple deduction, the absolute amplitude of the bright mode can be described as:

$$a = \frac{\omega_2^2 + i\gamma_2\omega - \omega^2}{(\omega_1^2 + i\gamma_1\omega - \omega^2)(\omega_2^2 + i\gamma_2\omega - \omega^2) - \kappa^2} E_0 \quad (3)$$

Now we assume the conditions $\gamma_2 << \gamma_1 << \omega_1, \omega_2$ and our interest lies in the frequency range around the dark mode excitation position. Thus the term $w_1^2 + ig_1 w - w^2$ can be considered as a constant and the transmission spectrum can easily be plotted using the above equation. For example, we consider the bright molecule to resonate at a frequency ω_1 =1.0 THz with a damping rate γ_1 =0.2 THz coupled to the dark molecule oscillating at a frequency ω_2 =1.1 THz with a damping rate γ_2 =0.005 THz. The coupling coefficient is set to be 0.05 and the incident electric field amplitude is normalized to unity. As we can see from Fig. 7(b), the bright mode (black line) exhibits a broad band resonance with high radiation loss which is contained in the variable γ_1 in the equation, while the dark mode (red line) shows a narrow band resonance with low damping rate. It should be mentioned that, in the ideal case the dark mode should possess no loss, which means that γ_2 =0 and the spectrum for this mode is described by the Dirac function. When these two modes couple with each other, a new asymmetric Fano resonance can be produced with narrow band-width near the dark mode position. Furthermore, when the eigen-frequency of the dark mode is overlapping with the bright mode, a transparency window appear in the middle of transmission minimum (see Fig. 7(c)). Interestingly, due to the huge difference of the damping rate, the line-shape of the Fano resonances can be expressed as the second derivative of the original bright mode spectrum. From the above discussion, we can conclude that Fano resonance in our asymmetric THz metamaterials could be generally explained by mode coupling. This description is not limited to the metamaterials region, but also applies in plasmonic mode coupling with various configurations. However, it has been proposed that no dark mode excitation is necessary for the generation of Fano resonances and the dark mode can be excited directly with zigzag-shaped metasurfaces [34], which are beyond the scope of our study.

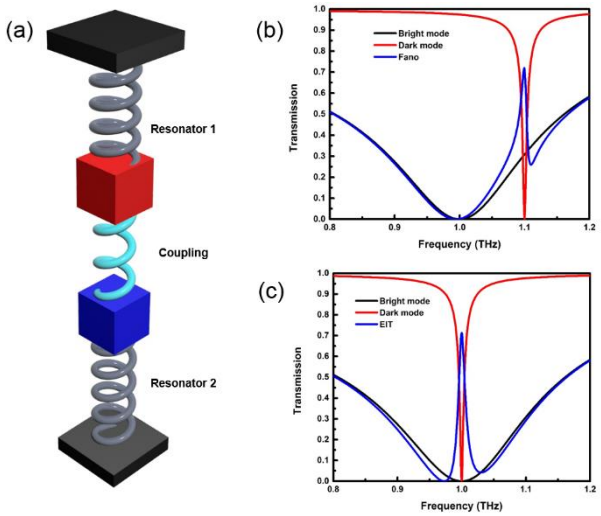

Fig. 7 (a) Schematic illustration of the equivalent coupled oscillator model, in which bright and dark mode is oscillating at frequency ω_1 and ω_2, with a different damping rate γ_1 and γ_2, respectively. The coupling coefficient is κ. (b) Fano resonance and (c) EIT-like effect can be generated with simple coupled mode analysis.

5. ACTIVE TUNING OF FANO RESONANCES

In order to explore the tuning capabilities of our Fano resonances generated in asymmetric THz metamaterials, we study the thermal tunability of a liquid crystal infiltrated structure, as shown in Fig. 8(a). With ebeam-lithography, the eSRR are made of 10 nm thick titanium and 200 nm thick gold deposited on 1mm-thick z-cut quartz substrate. The width of all bars in the unit cell is 4 μm and the gap is 2 μm wide. Our metamaterials with lateral dimension of 36 μm in both directions and form a square lattice with the period of 50 μm. The mirror symmetry of the meta-structure is broken by shifting the side gaps of 4 μm. In order to fabricate metallic structure on insulating substrate such as quartz, an addition process should be added before conducting the e-beam lithography. Evaporation of 20 nm thick aluminium on the baked resist can prevent the accumulation of charges on the substrate and deform of the fabricated pattern. The overall sample size patterned with metamaterial pattern is 20 mm by 20 mm.

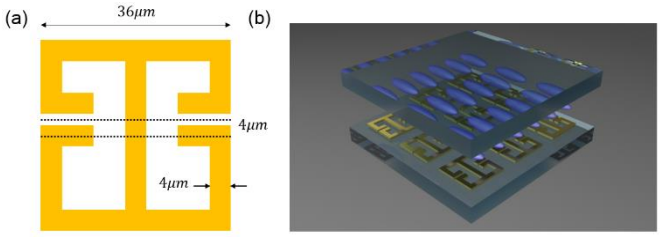

Fig. 8 (a) Schematic top view of the metamaterial unit cell. (b) 3D view of the liquid crystal-metamaterial cell. The eSRR is fabricated on top of quartz plate while covered with a thin layer of alignment polyimide. The inner side of top quartz is also coated with alignment layer which is mechanically brushed.

The liquid crystal mixture we use is E7 (Merck KGaA, Germany) and they are infiltrated between the asymmetric eSRR and an additional 1-mm-thick quartz plate (see the 3D schematic view of the structure in Fig. 8(b)). Before filling the liquid crystal material in the cell, a layer of polyimide is used as alignment by spin-coating on the inner side of each quartz plate and mechanically rubbed with microfiber cloth. The orientation of the aligned liquid crystal molecules is perpendicular to the direction of the gap and parallel to the incident THz wave polarization at room temperature. Dielectric spacers are sandwiched between two quartz plates and their thickness is 10 μm. The sealed cell is mounted on a temperature controller touching the quartz plate and a dc power supply is used for the heating of the cell. At room temperature, the liquid crystal is characterized by the extraordinary index n_e. With the increase of temperature, we increase the internal energy of liquid crystal and the molecules go through nematic-isotropic transition with random distributions of directors. At isotropic state, the liquid crystal is polarization independent and the refractive index can be expressed as $n = n_e / 3 + 2n_o / 3$, where n_o represents the ordinary refractive index.

Simulations are performed using the commercial available full-wave software Lumerical FDTD solutions. In our simulation, normal incident THz waves is used with polarization across the gap of the metamaterial resonator. Liquid crystal materials is considered bulk materials with frequency independent refractive index $n_e = 1.74$ and $n_o = 1.60$. The boundary conditions in the simulation were periodic conditions for in plane directions and perfectly matched layer (PML) for out-of-plane direction. The simulated time is 100 ps and the corresponding frequency resolution is 2.0 GHz. Fig. 9 shows the broadband THz transmission through the device with the liquid crystal in nematic and isotropic phase, respectively. As discussed in previous section, there are three resonance dips relating to the excitation of three different modes in the SRR metamaterial when there is no liquid crystal infiltration. A narrow resonant dip at 0.50 THz corresponds to the LC mode where two close loop current circulate in the opposite direction and generate zero net magnetic field. A broadband resonance occurred at 2.07 THz is related to the dipole mode where the electric current flows in the direction of the incident THz polarization. A new transmission minimum can be observed at 1.48 THz, which is the Fano resonance generated by mirror-symmetry-breaking at y axis. At this resonance dip, four sub-loop surface current flows in clockwise or anti-clockwise directions. When the surface of metamaterials is covered with 10 μm thick liquid crystal molecules, the whole spectrum is squeezed towards low frequency. The Fano resonant dip at 1.48 THz is shifted to 1.30 THz when the polarization is in y-direction and 1.32 THz when the liquid crystal is in isotropic phase. It should be mentioned that the absorption of liquid crystals is not considered in the simulation.

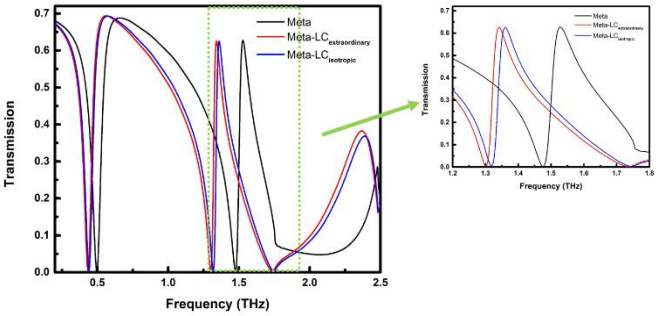

Fig. 9. Simulated THz transmission spectrum of liquid crystal-metamaterial device. The graph on the right is the device response of the amplified green region. The transmission spectrum undergoes red-shift when the device is covered with liquid crystal.

The thermal tuning of liquid crystal infiltrated device is performed with a standard THz-TDS setup. The bare quartz reference and the sample are placed on a temperature control stage embedded in the TDS chamber. Dry nitrogen is purged into the chamber to remove the water vapour which causes absorption along the THz path. Using two parabolic off-axis mirrors, the terahertz pulses are guided and focused onto the samples. A coherent detection employs electro-optical sampling with a ZnTe crystal, which allows the detection of both amplitude and phase of the transmitted THz wave. As the temperature increase or decrease, thermal equilibrium is reached before conducting any TDS measurement. The total scanning time of the measured THz pulse is 50 ps. The measured temperature dependent THz transmission is shown in Fig. 10, from which we can clearly observe a frequency blue-shift for both the LC and Fano resonances, when the temperature is raised from 23°C to 100°C. Especially, the Fano resonance dip is shifted from 1.44 THz to 1.49 THz, representing a frequency shift of 50 GHz, which is larger than the simulated result. This difference is attributed to the limited frequency resolution of the TDS measurement and the fabrication error. The inset graph illustrates the time-domain signal measured at room temperature and the main pulse is followed by amplitude oscillation induced by resonances in metamaterial structure. In addition, there are other pulses appearing due to the multi-reflection of THz waves in the quartz substrate. When processing the data, we choose a 16 picosecond time-domain window to cut off the Fabry-Perot resonance (Fig. 10 inset). To some extent, this procedure would compromise the detected Q-factor of SRR resonances because other SRR induced oscillation tails left out the window are not considered. For the same reason, the frequency resolution in our measurement (18 GHz) causes difficulty in differentiating the small frequency shift due to the changing temperature. Despite that, we can clearly see the sensitivity of asymmetry induced Fano resonances (50 GHz frequency shift) on surrounding environment, while the maximum frequency shift for the LC mode is 18 GHz. The spectral shift reported in this work is larger than previous ones, which have a frequency tuning of 30 GHz by using liquid crystals loaded THz metamaterials [35,36].

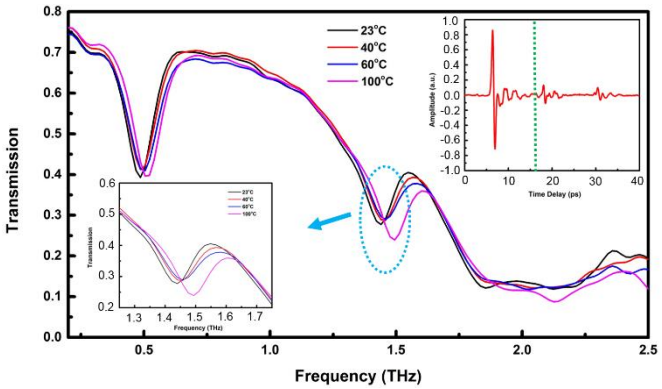

Fig. 10. Experimentally measured transmission coefficient of liquid crystal infiltrated metamaterial device at different temperatures. The inset in the left exhibits the amplified view of the Fano resonance region, while the inset in the right shows the measured time-domain signal at 23°C and the dashed line represents the cut-off window.

By using a liquid crystal infiltrated asymmetric eSRR structure, we are able to actively tune the frequency response of Fano resonances with a maximum frequency shift of 50 GHz for THz wave polarized along the y-axis. The small difference between the simulation and experimental result originate from the metamaterial fabrication errors, the imperfect alignment of liquid crystal materials and most importantly, the limited frequency resolution in our THz-TDS system. In addition, the resonance frequency shift can be explained from a simple qualitative model. When the refractive index of the material surrounding a resonator increases, the effective wavelength of the THz wave travelling required for the resonance becomes larger, e.g. in Fabry-Perot resonator. Therefore, the resonance would shift to the low frequency side. E7 mixture has positive anisotropy, which means the refractive index of extraordinary state is larger than that of ordinary/isotropic state ($n_e > n_{isotropic} > n_o > n_{air}$). This intuitive theory is consistent with our simulated and experimental demonstrations.

The asymmetric THz metamaterials analyzed in this paper can provide straightforward application in different areas. Small perturbations of the background, geometric structure and intrinsic material parameters could induce the spectral shift of the Fano resonances, and this can easily be implemented for chemical or biological sensor applications. Also due to the large wavelength (in THz region) and the inherent interaction between THz radiation and materials, this kind of device could potentially be used in various environments. Moreover, from Babinet's principle [36], complementary THz metamaterials should possess reverse Fano transmission features. Asymmetry induced Fano resonant peaks instead of dips will be observed in transmission spectra when asymmetry is introduced into the unit cells. In addition, the structure in our paper is not optimized for specific purposes and can apply for different scenarios. For example, a controllable high Q-factor resonance could be used for compressed imaging in the frequency domain.

6. SUMMARY

We have demonstrated through simulation and experiment that Fano resonance and EIT-like phenomenon can easily be generated by breaking the mirror symmetry of THz metamaterial unit cells in either of the in-plane directions. Six THz metamaterial designs have been evaluated by breaking mirror-symmetry. Ultra-sharp asymmetric resonance and narrow transmission window may appear close to or overlap with the original LC, dipole or higher order metamaterial eigen-modes. Fano resonance produces highly confined electric fields and unique transmission line-shapes which have the potential to enhance light-matter interaction for different purposes, such as nonlinear responses. Surface current and Q-factor are discussed to understand the characteristic features lying in these resonances. The coupling between the high radiation loss bright mode and low damping dark mode is considered to be the mechanism for Fano resonances and EIT-like property. A simple coupled mode theory is introduced to explain the high Q-factor and asymmetric nature of the transmission line-shape. Moreover, we have demonstrated that Fano resonances generated from liquid crystal infiltrated symmetry-breaking THz metamaterials can be efficiently tuned by changing the phase of the liquid crystal. The ultra-narrowband Fano resonances enables high sensitivity of surrounding environment. These asymmetric metamaterials can provide new ways for highly sensitive biological or chemical detection.

ACKNOWLEDGMENT

The authors would like to thank the UK Engineering and Physical Sciences Research Council (EPSRC) for the support through the Platform Grant for Liquid Crystal Photonics (EP/F00897X/1). Xuefeng Li would like to acknowledge the support from Cambridge Trust.

REFERENCES

1. B. Ferguson and X.-C. Zhang, "Materials for terahertz science and technology.," Nat. Mater. **1**, 26–33 (2002).
2. M. Tonouchi, "Cutting-edge terahertz technology," Nat. Photonics **1**, 97–105 (2007).
3. Y. S. Lee, *Principles of Terahertz Science and Technology* (2009).
4. P. H. Siegel, "Terahertz technology," IEEE Trans. Microw. Theory Tech. **50**, (2002).
5. C. A. Schmuttenmaer, "Exploring dynamics in the far-infrared with terahertz spectroscopy," Chem. Rev. **104**, 1759–1779 (2004).
6. M. Exter, C. Fattinger, and D. Grischkowsky, "Terahertz time-domain spectroscopy of water vapor.," Opt. Lett. **14**, 1128–1130 (1989).
7. M. C. Beard, G. M. Turner, and C. A. Schmuttenmaer, "Transient photoconductivity in GaAs as measured by time-resolved terahertz spectroscopy," Phys. Rev. B - Condens. Matter Mater. Phys. **62**, 15764–15777 (2000).
8. P. H. Siegel, "Terahertz technology in biology and medicine," IEEE Trans. Microw. Theory Tech. **52**, 2438–2447 (2004).
9. R. Piesiewicz, T. Kleine-Ostmann, N. Krumbholz, D. Mittleman, M. Koch, J. Schoebei, and T. K??rner, "Short-range ultra-broadband terahertz communications: Concepts and perspectives," IEEE Antennas Propag. Mag. **49**, 24–39 (2007).
10. B. S. Williams, "Terahertz quantum-cascade lasers," Nat. Photonics **1**, 517–525 (2007).
11. M. Naftaly and R. E. Miles, "Terahertz Time-Domain Spectroscopy for Material Characterization," Proc. IEEE **95**, 1658–1665 (2007).
12. J. Valentine, S. Zhang, T. Zentgraf, E. Ulin-Avila, D. A. Genov, G. Bartal, and X. Zhang, "Three-dimensional optical metamaterial with a negative refractive index.," Nature **455**, 376–379 (2008).
13. D. Schurig, J. J. Mock, B. J. Justice, S. A. Cummer, J. B. Pendry, A. F. Starr, and D. R. Smith, "Metamaterial electromagnetic cloak at microwave frequencies.," Science **314**, 977–980 (2006).
14. N. Landy, S. Sajuyigbe, J. Mock, D. Smith, and W. Padilla, "Perfect Metamaterial Absorber," Phys. Rev. Lett. **100**, 207402 (2008).
15. A. V Kildishev, A. Boltasseva, and V. M. Shalaev, "Planar Photonics with Metasurfaces," Science (80-.). **339**, 1289 (2013).
16. N. Yu, P. Genevet, M. A. Kats, F. Aieta, J.-P. Tetienne, F. Capasso, and Z. Gaburro, "Light Propagation with Phase Discontinuities: Generalized Laws of Reflection and Refraction," Science (80-.). **334**, 333–337 (2011).
17. D. Shin, Y. Urzhumov, Y. Jung, G. Kang, S. Baek, M. Choi, H. Park, K. Kim, and D. R. Smith, "Broadband electromagnetic cloaking with smart metamaterials.," Nat. Commun. **3**, 1213 (2012).
18. P. Genevet, F. Aieta, M. a. Kats, R. Blanchard, G. Aoust, J.-P. Tetienne, Z. Gaburro, and F. Capasso, "Flat Optics: Controlling Wavefronts With Optical Antenna Metasurfaces," IEEE J. Sel. Top. Quantum Electron. **19**, 4700423–4700423 (2013).
19. D. K. Armani, T. J. Kippenberg, S. M. Spillane, and K. J. Vahala, "Ultra-high-Q toroid microcavity on a chip.," Nature **421**, 925–928 (2003).
20. R. Marqu??s, F. Mesa, J. Martel, and F. Medina, "Comparative Analysis of Edge- and Broadside-Coupled Split Ring Resonators for Metamaterial Design - Theory and Experiments," IEEE Trans. Antennas Propag. **51**, 2572–2581 (2003).
21. V. Fedotov, M. Rose, S. Prosvirnin, N. Papasimakis, and N. Zheludev, "Sharp Trapped-Mode Resonances in Planar Metamaterials with a Broken Structural Symmetry," Phys. Rev. Lett. **99**, 147401 (2007).
22. W. Cao, R. Singh, I. a I. Al-Naib, M. He, A. J. Taylor, and W. Zhang, "Low-loss ultra-high-Q dark mode plasmonic Fano metamaterials.," Opt. Lett. **37**, 3366–8 (2012).
23. B. Luk'yanchuk, N. I. Zheludev, S. a Maier, N. J. Halas, P. Nordlander, H. Giessen, and C. T. Chong, "The Fano resonance in plasmonic nanostructures and metamaterials.," Nat. Mater. **9**, 707–15 (2010).
24. R. Singh, I. A. I. Al-Naib, M. Koch, and W. Zhang, "Sharp Fano resonances in THz metamaterials," Opt. Express **19**, 6312–6319 (2011).
25. R. Singh, I. A. I. Al-Naib, Y. Yang, D. R. Chowdhury, W. Cao, C. Rockstuhl, T. Ozaki, R. Morandotti, and W. Zhang, "Observing metamaterial induced transparency in individual Fano resonators with broken symmetry," Appl. Phys. Lett. **99**, 201107 (2011).
26. R. Singh, I. Al-Naib, W. Cao, C. Rockstuhl, M. Koch, and W. Zhang, "The Fano resonance in symmetry broken terahertz metamaterials," Terahertz Sci. Technol. IEEE Trans. **3**, 820–826 (2013).
27. R. Singh, W. Cao, I. Al-Naib, L. Cong, W. Withayachumnankul, and W. Zhang, "Ultrasensitive terahertz sensing with high-Q Fano resonances in metasurfaces," Appl. Phys. Lett. **105**, 171101 (2014).
28. A. E. Miroshnichenko, S. Flach, and Y. S. Kivshar, "Fano resonances in nanoscale structures," Rev. Mod. Phys. **82**, 2257–2298 (2010).
29. C. Wu, A. B. Khanikaev, R. Adato, N. Arju, A. A. Yanik, H. Altug, and G. Shvets, "Fano-resonant asymmetric metamaterials for ultrasensitive spectroscopy and identification of molecular monolayers," Nat. Mater. **11**, 69–75 (2011).

30. D. Schurig, J. J. Mock, and D. R. Smith, "Electric-field-coupled resonators for negative permittivity metamaterials," Appl. Phys. Lett. **88**, 1–3 (2006).
31. H.-T. Chen, J. F. O'Hara, A. J. Taylor, R. D. Averitt, C. Highstrete, M. Lee, and W. J. Padilla, "Complementary planar terahertz metamaterials.," Opt. Express **15**, 1084–95 (2007).
32. L. Cong, M. Manjappa, N. Xu, I. Al-Naib, W. Zhang, and R. Singh, "Fano Resonances in Terahertz Metasurfaces: A Figure of Merit Optimization," Adv. Opt. Mater. **3**, 1537–1543 (2015).
33. N. Liu, L. Langguth, T. Weiss, J. Kästel, M. Fleischhauer, T. Pfau, and H. Giessen, "Plasmonic analogue of electromagnetically induced transparency at the Drude damping limit.," Nat. Mater. **8**, 758–762 (2009).
34. S. Burokur, A. Lupu, and A. de Lustrac, "Direct dark mode excitation by symmetry matching of a single-particle based metasurface," arXiv Prepr. arXiv1406.6378 1–21 (2014).
35. O. Buchnev, J. Wallauer, M. Walther, M. Kaczmarek, N. I. Zheludev, and V. A. Fedotov, " Controlling Intensity and Phase of Terahertz Radiation with an Optically Thin Liquid Crystal-Loaded Metamaterial," Appl. Phys. Lett. 103, 141904 (2013)
36. S. Savo, D. Shrekenhamer and W. J. Padilla, " Liquid Crystal Metamaterial Absorber Spatial Light Modulator for THz Applications," Adv. Opt. Mater. 2, 275 (2014)
37. F. Falcone, T. Lopetegi, M. Laso, J. Baena, J. Bonache, M. Beruete, R. Marqués, F. Martín, and M. Sorolla, "Babinet Principle Applied to the Design of Metasurfaces and Metamaterials," Phys. Rev. Lett. **93**, 197401 (2004).